Synthetic Aperture Radar Based Spacecraft Terrain Relative Navigation

Bryan S. Pogorelsky*, Renato Zanetti† and Jingyi Chen‡
The University of Texas at Austin, Austin, Texas, 78712

Scott Jenkins§
Sandia National Laboratories, Albuquerque, New Mexico, 87123

A spacecraft terrain relative navigation system for Low Elevation Orbit satellites is presented relying on measurements obtained from a synthetic aperture radar (SAR) that are fused with inertial measurements and attitude determination system data in a multiplicative extended Kalman filter. Techniques such as autofocusing and geocoding are employed to retrieve information from SAR images for incorporation into the navigation filter. Monte Carlo simulation results are presented in which actual filter performance is compared to predicted filter performance. Specifically, two test cases, with varied initial SAR antenna misalignment uncertainty, show that the SAR based terrain relative navigation system is a valid approach to GPS-denied navigation.

Nomenclature

$\mathbf{a}$	=	Spacecraft's acceleration vector
$\mathbf{B}$	=	Geolocation error contribution covariance
c	=	Speed of light
$\mathbf{D}$	=	Center pixel covariance matrix
dr	=	Range spacing
$\mathbf{F}$	=	Jacobian of state dynamics
f_s	=	Range sample frequency
$\mathbf{G}$	=	Noise shaping matrix
$\mathbf{g}$	=	Mass attraction acceleration
$\bar{g}$	=	Average pixel intensity
$\mathbf{g}_\mathrm{l}$	=	Local gravity vector

---

*Graduate Research Assistant, Aerospace Engineering and Engineering Mechanics.
†Assistant Professor, Aerospace Engineering and Engineering Mechanics, AIAA Associate Fellow.
‡Assistant Professor, Aerospace Engineering and Engineering Mechanics.
§Engineer, Dept. 5322 (NPC and Systems Integration).

$\mathbf{H}$	=	Measurement mapping matrix
$\tilde{\mathbf{H}}$	=	Jacobian of measurement model with respect to center pixel
i	=	Image width index
j	=	Image height index
k	=	Time step
k_c	=	Index of center range line
$\mathbf{K}$	=	Kalman gain
M	=	Image width
N	=	Image height
$\mathbf{P}$	=	Estimation error covariance
$\mathbf{Q}_{\mathrm{PSD}}$	=	Process noise spectral density
$\mathbf{q}_\mu$	=	SAR antenna misalignment with spacecraft body quaternion
$\mathbf{R}$	=	Measurement error covariance
$\mathbf{R}'$	=	Adjusted measurement error covariance
$\mathbf{r}$	=	Spacecraft's position vector
$\|\mathbf{r}_{\mathrm{s,f}}\|$	=	Slant range
r_0	=	Measured near range
$\mathbf{S}$	=	Innovation covariance
$\mathbf{T}$	=	Direction Cosine Matrix
t	=	Time
$\mathbf{v}$	=	Spacecraft's velocity vector
v_{ic}	=	In-track velocity component
$\mathbf{x}$	=	True state vector
$\hat{\mathbf{x}}$	=	Estimated state vector
x_{s}	=	X-component of antenna to feature vector in the antenna frame
$\mathbf{y}$	=	Measurement vector
$\tilde{\mathbf{y}}$	=	Pre-fit residual
y_{s}	=	Y-component of antenna to feature vector in the antenna frame
z_{s}	=	Z-component of antenna to feature vector in the antenna frame
$\bar{\beta}$	=	Underweighting scaling factor
γ	=	Underweighting threshold
$\delta\boldsymbol{\mu}$	=	Antenna misalignment error

μ	=	SAR antenna misalignment with spacecraft body
σ	=	Standard deviation
ϕ_m	=	Ratio measurement
ω	=	Rotation rate

Subscripts

b	=	Spacecraft body frame
e	=	ECEF frame
f	=	Center pixel feature
s	=	SAR antenna frame

Functions

$g(\cdot,\cdot)$	=	Function returning pixel intensity
$h(x)$	=	Measurement model
$[\cdot\times]$	=	Function returning the cross product skew symmetric matrix

I. Introduction

WHEN a spacecraft cannot rely on ground stations or global navigation satellite systems, such as GPS, terrain relative navigation (TRN) is a method that can be employed to obtain accurate onboard navigation solutions. The basic functionality of TRN is to aid inertial navigation systems (INS) by providing relative position or bearing information to known surface features.

Data acquired from various sensor types have been used for TRN, including radar altimeters as in the case of the Terrain Contour Matching System (TERCOM) [1], passive optical cameras employed in the Autonomous Precision Landing Navigation system (APLNav) [2], and LIDAR in NASA's Autonomous Landing Hazard Avoidance Technology (ALHAT) project for lunar landing [3]. *A priori* reference maps, such as digital elevation maps (DEMs) or optical images with scaling information, are required to perform TRN. These reference maps can be created pre-flight or during the mission, as done by the Dawn spacecraft [4].

Each sensors type has advantages and disadvantages. For example, optical imagery provides large amounts of spatial coverage but can be negatively impacted by adverse light, cloud, or weather conditions. Radar altimeters, while being able to function in most weather and lighting conditions, require the collection of long contours for geolocation [5]. Technologies such as flash LIDAR can collect a grid of range measurements to be used for correlation with DEMs, but are generally limited in their effective range when used for TRN. The ALHAT flash LIDAR for example has an operational range of 1800 m to 20 km when the number of illuminated pixels is reduced from 128×128 to 11×11 and a spatial resolution of up to 10 cm [6] . This range is not sufficient for performing terrain relative navigation at altitudes

experienced in low Earth orbit. Synthetic Aperture Radar (SAR) is an imaging radar that is widely used for remote sensing science applications as well as military surveillance and reconnaissance activities. Using SAR for navigation purposes presents some compelling advantages over the sensors outlined above. SAR receives radar echoes independent of lighting or weather conditions from large distances and with high spatial resolution, on the order of 5 to 30 meters, comparable for example to the 30 meter resolution of visible spectrum Operational Land Imager on Landsat 8 [7]. This has been successfully demonstrated in a variety of orbital applications such as Seasat [8], the Shuttle Radar Topography Mission (SRTM) [9], and Sentinel-1 [10]. SAR based navigation blends many of the advantages of flash LIDAR, radar altimetry, and optical sensors in that it can collect radar imagery with range information from large distances and in many environmental conditions.

Previous studies have been conducted in the use of SAR for terrain relative navigation. Bevington and Marttila [11] proposed obtaining aircraft position updates for an inertial navigation system with imagery gathered from a synthetic aperture radar. A dynamic programming approach was implemented to match linear features (such as roads) from optical images to corresponding linear features in the SAR images. To test the performance of this system, open-loop navigation and feature prediction/extraction performance were evaluated separately. Open-loop navigation refers to the fact that SAR sensor-based measurement updates were modeled as point fixes with errors and were not obtained from SAR images derived from an INS solution. This resulted in position accuracies on the order of tens of meters. An important caveat of SAR image processing is that knowledge is needed of the imaging platform's state, where particular state components required vary according to the processing technique used, for production of high-quality images. This presents a challenge to performing closed-loop navigation, where SAR based measurements are dependent on INS solutions. Paschall and Layne [12] investigated an INS, GPS, and SAR targeting system where SAR derived measurements were fed into a Kalman filter. Monopulse measurements were also integrated into this system to provide complete angle information to targets. Additionally, no image correlation was performed, thus accurate knowledge of landmark locations was needed for SAR aided navigation to be effective. More recently, work by Doerry [13] and Doerry et al.[14] describe methods of using SAR images to estimate IMU heading errors and radar velocity respectively, where the information could ultimately be fed into a navigation filter.

Nitti et al [15] provide a feasibility analysis of using an unmanned aerial vehicle (UAV) mounted SAR instrument with an automatic target recognition system to match features in an amplitude image with those found in a database to be used for georeferencing. No direct simulations were conducted, but performance bounds were established with errors limited to within 12 meters. Work by Kim et al. [16] proposed using interferometric synthetic aperture radars (InSARs) in conjunction with stored DEMs. The process entails taking InSAR measurements from the closest point on the ground and search for that same point on the DEM yielding measurement residuals. The measurement residuals are then incorporated in a particle filter to provide a state estimate. To validate the performance of the algorithm, the InSAR measurements were generated from an already existing DEM and not from actual SAR radar returns. While this method

did provide sub 10 meter RMS position errors in simulation a major drawback of using InSAR for TRN is the fact that to generate interferometric radar altimeter measurements is that a phase difference between signals received from two or more antennas located at different locations on the imaging platform needs to be received. Christensen et al [17] correlate the similarity of a SAR image generated with the back-propagation algorithm in the presence of navigation errors with an error-free SAR image of the same location. This correlation is used to update the navigation state.

Lindstrom et al [18] investigated using SAR range and range-rate measurements to perform GPS-denied navigation for an airborne platform with an IMU used for state propagation between measurements. In addition to range and range-rate, altitude measurements (from an altimeter) are also taken into account in an EKF to remove an ambiguity in the processing methodology used. It is assumed that the absolute location of the specific ground target is known *a priori*. Simulations were performed to investigate sensitivity to IMU grade, SAR measurement noise, and relative target location to overall navigation performance concluding in the fact that their proposed system could be feasible with either navigation or tactical grade IMUs [19] with optimal performance occurring when ground targets are closer to the flight trajectory. As the use of machine learning techniques has increased in popularity significantly in the last decade, its application for terrain relative navigation has also been explored. White et al. [20] proposed a neural network approach for recovering a true flight trajectory from errors in online-generated SAR images. The process uses a convolutional neural network (CNN) where the inputs are a distorted image and a reference image act as inputs from which initial position and velocity errors are recovered. These initial conditions can than be propagated (under the assumption of straight and level flight) to reconstruct an entire trajectory. Performance was found to improve with increasing synthetic aperture length, with the CNN properly characterizing blurring in the generated images with the correct error source.

This works seeks to develop an approach to SAR based terrain relative navigation for space based platforms. Additionally, this is done without the use of external aiding, namely GPS, while removing some limitations of the studies mentioned above such as feature matching only being applied to linear features. Most importantly, closed-loop navigation simulations are performed where SAR derived measurements are reliant on the navigation solution, and conversely, the navigation solution is reliant on the SAR derived measurements.

The remainder of this paper is structured as follows: An overall system overview is first presented in Section II and the SAR image generation process is described in Section III. Section IV covers the image geolocation process followed by a description of the multiplicative extended Kalman filter in Section V. Details of the TRN numerical simulation with corresponding results are shown in Section VI and VII respectively. Finally, concluding remarks on the methodology and results are found in Section VII

II. System Overview

The proposed system consists of four major steps: SAR image formation, SAR image geolocation, INS state propagation, and finally an EKF measurement update. Figure 1 below shows the system architecture and flow of the
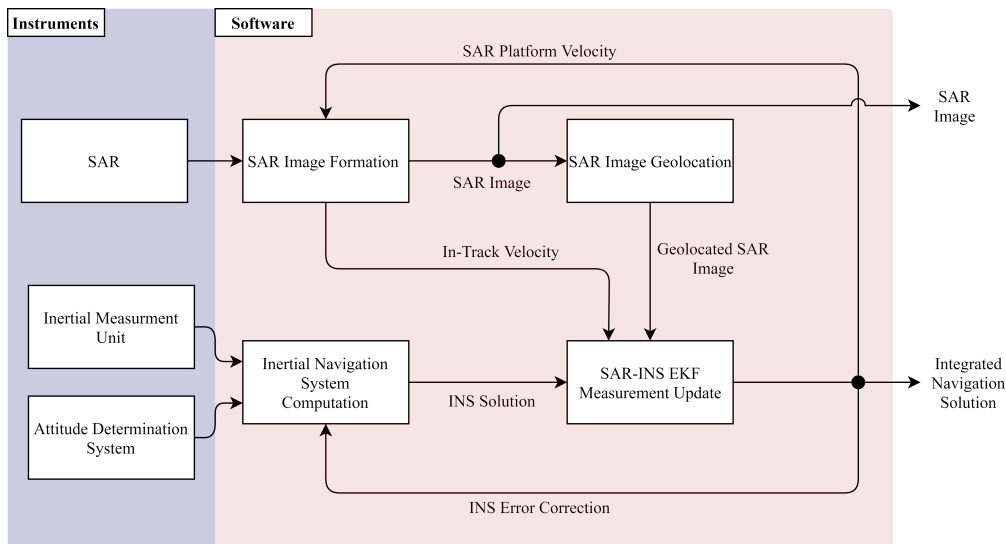
navigation process.

Fig. 1 Integrated SAR-INS architecture

A multiplicative extended Kalman filter (MEKF) is used with states for spacecraft position, velocity, and SAR antenna misalignment. To estimate in-track velocity errors, an autofocusing algorithm (with in-track velocity as the tuning parameter) is implemented to form a well-focused SAR image. Geolocation is done by co-registering the center pixel of the SAR image with a geocoded reference SAR image using a feature matching algorithm. The Earth-centered, Earth-fixed (ECEF) coordinate of the center pixel of the image is then extracted along with the slant range to that pixel. From the autofocusing step, an estimate of the spacecraft's in-track velocity is used as an additional measurement. These are then utilized in the MEKF to produce the final navigation solution.

III. SAR Image Formation

A. SAR Overview

SAR systems send out pulses of sequential electromagnetic waves and collect backscattered echoes. Every transmission/reception corresponds to different positions due to the movement of the platform; an appropriate coherent combination of the received signals creates the "synthetic aperture". This synthetic aperture is much larger than the physical antenna length, allowing it to achieve high spatial resolution [21]. For the purposes of this paper, all SAR data is being collected in a stripmap mode. This means that the antenna stays fixed relative to the moving platform and is not being actively gimbaled during flight to "spotlight" a specific area on the ground. SAR imaging requires a side-looking geometry where the antenna either faces in a direction perfectly orthogonal to the flight path, a zero squint angle, or can have a forward or backward squint to varying magnitudes. Nevertheless, the general geometry remains side-looking and is required for the image formation technique used in the following section. A graphic of a SAR imaging geometry with

no squint can be seen below in Figure 2. The two properties of SAR that are exploited in this work are the amplitude
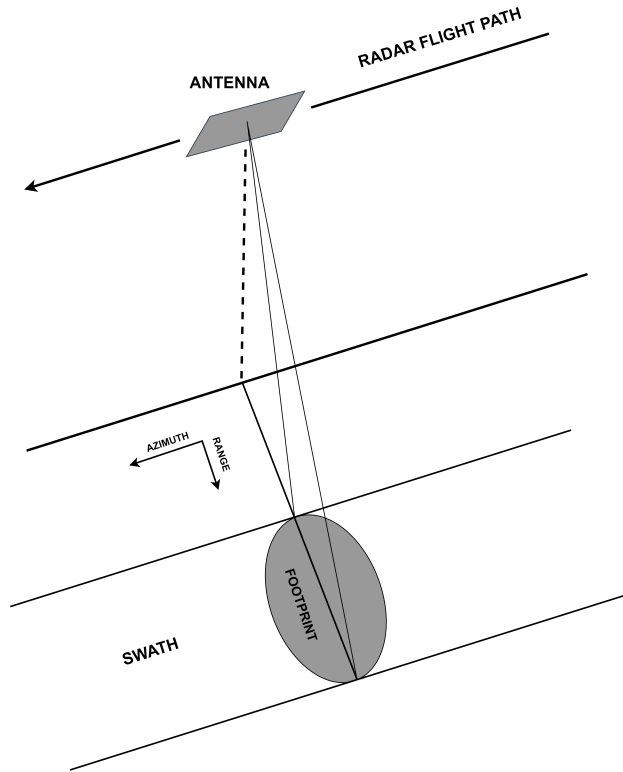

Fig. 2   SAR imaging configuration

image itself (used for geolocation) and the corresponding range information. An important quantity that one can retrieve from SAR data is the slant range (or line-of-sight distance) from the antenna to a pixel on the ground. For example, the slant range to the center pixel of an image can be written as,

$$\text{Slant Range} = r_0 + (k_c - 1)dr \tag{1}$$

where k_c is the index of the center range line and r_0 is the measured near range. The range spacing is calculated as,

$$dr = \frac{c}{2}\frac{1}{f_s} \tag{2}$$

where c is the speed of light and f_s radar range sample frequency.

B. SAR Image Formation

Radar images are complex-valued, meaning that each pixel has both an amplitude and a phase. Received radar echos are first compressed in the range direction through range modulation. Similarly, azimuth compression can be achieved by designing an azimuth matched filter based on the Doppler history of an point scatterer. In practice, range

and azimuth compression can be efficiently implemented using a Fast Fourier Transform (FFT). More details of the SAR image processing technique can be found in Reference 22.

The frequency domain approach used in this work requires knowledge of the in-track velocity in radar coordinates to properly focus a SAR image. Additionally, if there are significant out of track velocities the image may become defocused if techniques such as autofocusing are not applied. If image sharpness is significantly degraded due to incorrect knowledge of in-track velocity, subsequent geolocation steps can fail leading to the absence of filter measurement updates. In this paper it is assumed that degradation of SAR image quality only arises from in-track velocity due to the frequency-domain processing method outlined above. The satellite's velocity is available from the navigation system in the ECEF frame, hence i. knowledge of the satellite's attitude is needed to coordinatize the velocity in radar coordinates and ii. the navigation measurement extracted from the image is correlated to the navigation state.

Two SAR images are seen in Figure 3 below demonstrating the effects of in-track velocity error. Both are generated from L-band ALOS PALSAR data (available at the Alaska Satellite Facility Distributed Active Archive Center [23]) collected over the Houston area of the United States. This ALOS data has accurate orbit information which nominally produces focused images. To generate the image with in-track error, certain parameters in the processing software are altered to perturb the assumed in-track velocity by 15 m/s. To alleviate these type of errors, a hill climbing algorithm is
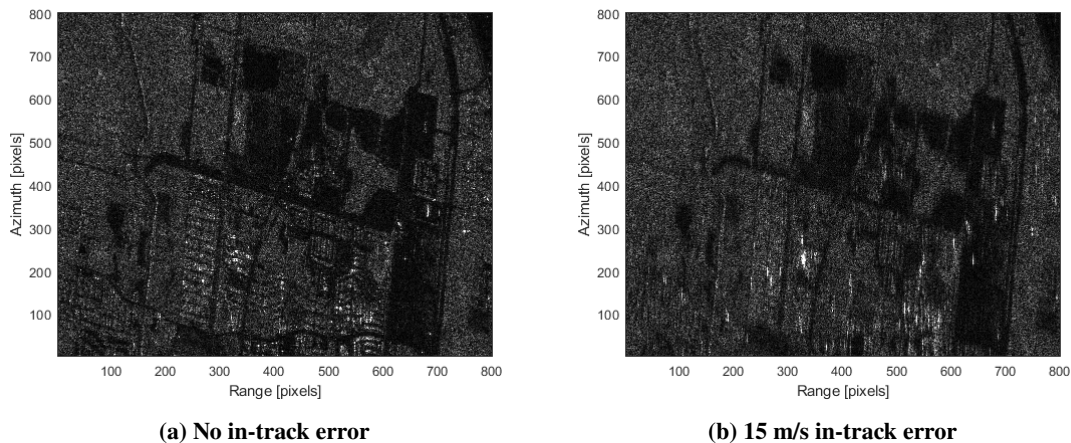

(a) No in-track error   (b) 15 m/s in-track error

Fig. 3   Impact of in-track velocity error on SAR image quality

used to find an in-track velocity value that maximizes the resulting image sharpness. The sharpness metric used for focusing is normalized variance [24],

$$\text{Sharpness} \equiv \frac{1}{MN\bar{g}^2} \sum_M \sum_N [g(i,j) - \bar{g}]^2 \tag{3}$$

where the image is $M \times N$ pixels with an individual pixel intensity, $g(i,j)$, and an average pixel intensity $\bar{g}$. A representative image sharpness curve is seen in Figure 4.
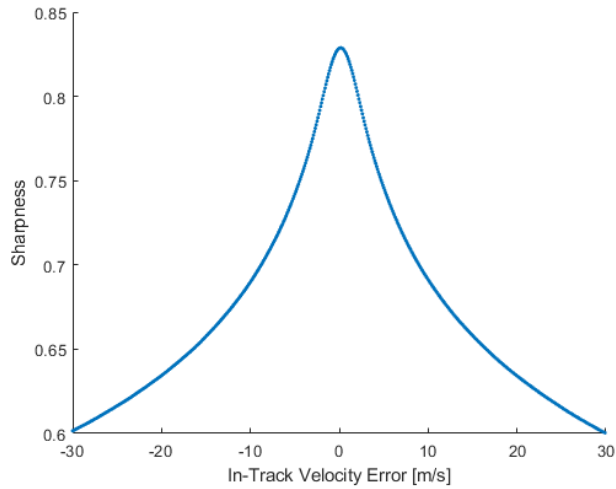
Fig. 4   Image sharpness curve

Hill climbing algorithms are a class of derivative-free optimization methods. The hill climbing algorithm functions by "stepping" in the direction that maximizes a cost function, normalized variance in this case, until no more improvement is gained. The constant velocity step size is treated as a user selected parameter that is chosen based on how much in-track velocity error is expected and the allowable computation time of focusing. Details of the algorithm can be seen below.

Algorithm 1: Autofocus Hill Climbing

---

inputs: unfocused image, initial estimate of in-track velocity, step size;
initialize parameters;
determine direction of increasing sharpness;
if neither direction increases sharpness **then**
    | new velocity = old velocity;
else
    | **while** iteration < maximum iterations **do**
    | new velocity = old velocity ± step size;
    | generate image with new velocity;
    | new sharpness = normalized variance of image;
    | **if** new sharpness < old sharpness **then**
    | new velocity = old velocity;
    | break;
    | **else**
    | old velocity = new velocity;
    | old sharpness = new sharpness;
    | continue;
    | **end**
    | **end**
end
generate autofocused image with new velocity;

In addition to providing focused images for the geolocation process, autofocusing serves as an important requirement

9

for the system as it relates to the EKF. A key assumption of the Kalman filter is that measurement errors are uncorrelated with state estimation errors. Images are not focused due to the navigation's errors in estimating in-track velocity which would increase the errors exhibited in measurements derived from the geolocated image, creating a direct dependency between the estimation error and the measurement error. By autofocusing, no matter how blurred the initially generated images are (within reason) due errors in the estimated in-track velocity, a focused image is produced which is uncorrelated with the navigation state used to initially produce it. The consistency of the EKF implementation shown in Section VII demonstrates that the correlation is effectively mitigated by this approach.

IV. Image Geolocation

Geolocation of the formed SAR image is done by co-registering it to a stored geocoded reference amplitude SAR image. This reference image covers a much larger general area of where the formed image is approximately expected to be. A geocoded SAR image refers to an image in which each pixel has an associated latitude and longitude.

To co-register the two images with each other, features need to be detected in both images and then subsequently matched. This is accomplished by using MATLAB's computer vision toolbox [25]. The Speeded Up Robust Features (SURF) point detector and descriptor is used [26]. This algorithm is both scale and rotation-invariant making it a good choice for this application as the formed image will always cover a much smaller land area than the reference and will often not have the same orientation. The basic input of the algorithm is a grayscale image and the output is an array of SURF features which include characteristics such as point locations, scale, strength, and orientation. The first step of the geolocation process is to detect SURF features in each grayscale image.

After the SURF feature points are detected, putative point matches are made which may include outliers, or features that have a low likelihood of being correctly matched. The geometric transformation (mapping of inliers of one image to another) between the formed image and reference image is then found using the `estimateGeometricTransform` function in the toolbox which eliminates outliers using a random sample consensus algorithm. More details about this specific algorithm can be found in Torr et al. [27]. The type of transformation can be specified and for this application an affine transformation is selected. An affine transformation requires a minimum of three matched pairs of features, or the process will fail. Finally, using the transformation from the matched features, a bounding box on the reference image can be drawn. The nearest pixel to the location of the bounding box centroid is found, from which a latitude and longitude is retrieved, as the reference image is geocoded. The matched features and bounding box are seen in Figure 5. In this work all studies are conducted based on imagery collected from the same SAR platform. The formed image and reference image are captured from the same spacecraft, with the reference image being captured from a previous pass over the region of interest. Thus the resolution of the two image types is identical, with ones seen in Figure 5 as well as used in the subsequent section having a pixel size of 15 meters by 7.5 meters in the range and azimuth directions respectively. Such a specific setup is not a prerequisite for the image geolocation process to function. For
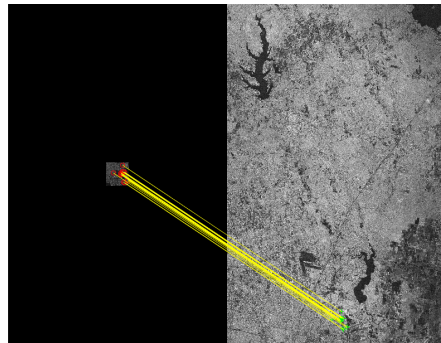
(a) Matched features between the formed and reference SAR images

(b) SAR image bounding box and centroid

Fig. 5   Co-registration of SAR images

example, it has been shown that image co-registration of images from the same sensor with SURF features can yield sub-pixel accuracy with image resolutions ranging from 30 meters to 2 meters [28]. Additionally, Liu et al. [29] have shown that SURF image matching with a random sample consensus algorithm can match SAR image features between images formed over different passes, different SAR systems, and varied resolutions (7 m vs 30 m). It is important to note that feature detection algorithms such as SURF and scale-invariant feature transform (SIFT) can be sensitive to speckle noise from images acquired at different times [30]. In this case, other SAR offset tracking techniques using complex cross-correlation (e.g. Strozzi et al. [31]) can be employed.   A limitation of the SURF feature matching method used in this work, and a majority of all terrain relative navigation approaches, is that it requires the observed ground area to have distinguishable features which can be matched between the stored reference data and collected data in-flight. For example, when the swath of the SAR antenna for a given image covers an ocean, desert, or dense forest no features can be extracted from either the reference image or collected image. During this time it is expected that such as system would simply propagate without measurement updates until the radar swath reaches an area of sufficiently distinguishable features. In this propagation-only phase, the estimation error may steadily increase due to un-modeled effects such as higher order spherical harmonics, solar radiation pressure, and atmospheric drag. Process noise is used to account for these un-modeled dynamics.

The latitude and longitude of a location on Earth is not enough to uniquely identify it, as its elevation is also needed. A stored digital elevation map of the larger area is used to determine the elevation of the point of interest. A search is

used to find the pixel on the DEM that is closest to the latitude and longitude of the center point. The corresponding height above the WGS 84 ellipsoid is then retrieved. Now with the latitude, longitude, and height (LLH) of the center pixel of the SAR image known, the ECEF coordinate of that point can be calculated using one of several methods of LLH to ECEF conversion.

V. Multiplicative Extended Kalman Filter

A 10 component (shown in Table 1) multiplicative extended Kalman filter is employed to estimate the states of the spacecraft. In this paper, states without subscripts or super scripts, such as $\mathbf{r}$ and $\mathbf{v}$, are assumed to be expressed in the

Table 1   Estimated states

State	# of Elements	Description
$\mathbf{r}$	3	spacecraft position in ECEF frame
$\mathbf{v}$	3	spacecraft velocity in ECEF frame
$\mathbf{q}_\mu$	4	SAR antenna misalignment with spacecraft body quaternion

ECEF frame. For example, $\mathbf{r}$ is a vector from the center of the earth to the spacecraft expressed in the ECEF frame. Subscripts and superscripts are also used, such as: $\mathbf{r}^c_{a,b}$. This would describe a vector from point a to b expressed in the c frame.

The notation used throughout this paper is to define $\mathbf{q}^b_a$ as the relative orientation quaternion between frames a and b. The quaternion is written as:

$$\mathbf{q}^b_a = \left[\left(\mathbf{q}^b_{a,v}\right)^T \quad q^b_{a,s} \right]^T \tag{4}$$

where $\mathbf{q}^b_{a,v}$ is the vector component and $q^b_{a,s}$ is the scalar component. The quaternion product, $\otimes$, that is adopted is Shuster's convention where rotations are interpreted as passive [32]. This is in the opposite order of Hamilton's composition, $\circledast$, where the rotations are treated as active [33]. The two differing compositions are related as follows,

$$\mathbf{p} \otimes \mathbf{q} = \mathbf{q} \circledast \mathbf{p} = \begin{bmatrix} p_s \mathbf{q}_v + q_s \mathbf{p}_v - \mathbf{p}_v \times \mathbf{q}_v \\ \\ p_s q_s - \mathbf{p}_v \cdot \mathbf{q}_v \end{bmatrix}. \tag{5}$$

The direction cosine matrix (DCM), otherwise known as a transformation matrix, can be obtained from a quaternion $\mathbf{q}$:

$$\mathbf{T}(\mathbf{q}) = \left(q^2_s - \mathbf{q}^T_v \mathbf{q}_v \right) \mathbf{I}_{3\times3} + 2\mathbf{q}_v \mathbf{q}^T_v - 2\mathbf{q}_s \left[\mathbf{q}_v \times \right], \tag{6}$$

where $[\mathbf{q}_v\times]$ is the skew-symmetric cross product equivalent matrix of the vector components of $\mathbf{q}$,

$$[\mathbf{q}_v\times] = \begin{bmatrix} 0 & -q_3 & q_2 \\ q_3 & 0 & -q_1 \\ -q_2 & q_1 & 0 \end{bmatrix}. \tag{7}$$

An EKF is chosen due to the nonlinear spacecraft dynamics and nonlinear measurement model used. The multiplicative EKF uses the non-singular quaternion representation of attitude, while deviations from the reference are three-component representations [34]. A number of simplifications are made regarding the geometry of the antenna in relation to the spacecraft. It is assumed that the antenna is rigidly attached to the spacecraft and that the center of the antenna is co-located with the center of mass of the vehicle. Additionally, the look and squint angles of the antenna are assumed to be known with some associated uncertainty (misalignment) yielding the nominal transformation between the antenna frame and spacecraft body frame. The look angle is measured from nadir up to the radar beam center, while the squint angle is measured from radar beam center to the normal of the flight path. The attitude of the spacecraft is assumed to be aligned with the local vertical, local horizontal (LVLH) frame at all times in its orbit and is known from an attitude determination system (ADS). Assuming a star-camera/gyro ADS, an attitude error on the order of tens of arcseconds is assumed negligible compared to the antenna misalignments. Finally, the analysis is done while the satellite is not maneuvering, such that all accelerometer measurements are not incorporated into the time propagation phase of the filter. In the context of this filter, measurements are gathered from the SAR instrument (and associated autofocusing) and not from the IMU or ADS. These are collected at fixed time increments which are much more spread apart than the high rate output of the IMU and ADS. Below, a three measurement collection is shown where measurement updates only occur at t_1, t_2, and t_3.
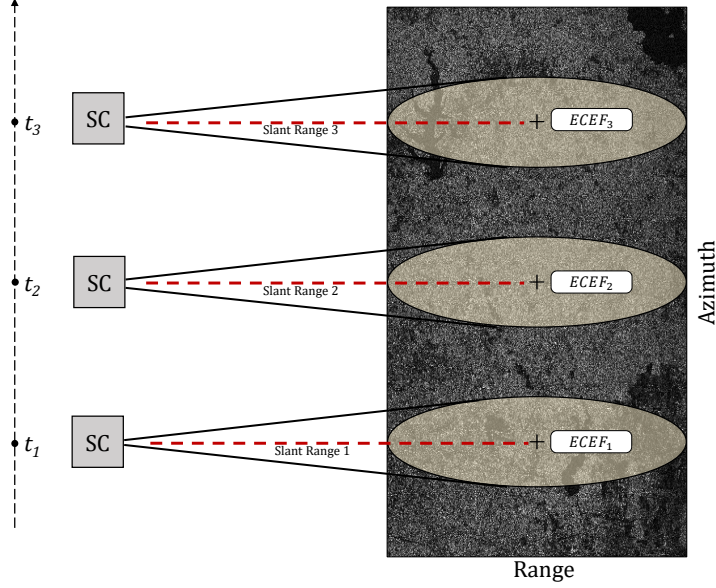
Fig. 6   Top view of SAR image collection

A. Time Propagation

Between SAR derived measurements, the states are propagated with IMU data in a process known as dead-reckoning. Since the position and velocity states are expressed in the ECEF frame, they are propagated in that same frame. This process is often referred to as ECEF mechanization and it is outlined below [35]. Propagation occurs discretely, where the time step, Δt, is the time difference between successive IMU/ADS measurements. Attitude information is received at fixed time increments from the ADS in terms of the quaternion from the ECEF frame to the body frame, $\mathbf{q}_e^b$, which is then converted to the corresponding DCM, $\mathbf{T}_e^b$, for use in subsequent calculations.

Next, the spacecraft acceleration in the ECEF frame, $\mathbf{a}_e$, is expressed as:

$$\mathbf{a}_{\mathrm{e}} = \left(\mathbf{T}_e^b\right)^T \mathbf{a}_{\mathrm{b}} - 2\omega_{\mathrm{ie}}^e \times \hat{\mathbf{v}}_{k-1}^+ + \mathbf{g}_{\mathrm{l}} \tag{8}$$

where $\mathbf{a}_b$ is the measured body acceleration, which is nominally zero in orbit when no maneuvers are occurring and ω_{ie}^e is the rotation rate of the earth expressed in the ECEF frame. The hat notation is used to show that a quantity is a filter's estimate and the minus/plus notations are used to show that the quantity is before/after the measurement update. The local gravity vector, $\mathbf{g}_{\mathrm{l}}$, is the sum of mass attraction acceleration, $\mathbf{g}$, and centripetal acceleration such that:

$$\mathbf{g}_{\mathrm{l}} = \mathbf{g} - \omega_{\mathrm{ie}}^e \times \left[\omega_{\mathrm{ie}}^e \times \hat{\mathbf{r}}_{k-1}^+\right]. \tag{9}$$

14

Velocity is updated using the previous estimate of the velocity with the acceleration calculated in Eq. (8),

$$\hat{\mathbf{v}}_k^- = \hat{\mathbf{v}}_{k-1}^+ + \mathbf{a}_e \Delta t. \tag{10}$$

Integrating the above equation, position is updated according to,

$$\hat{\mathbf{r}}_k^- = \hat{\mathbf{r}}_{k-1}^+ + \hat{\mathbf{v}}_{k-1}^+ \Delta t + \frac{1}{2} \mathbf{a}_e \Delta t^2. \tag{11}$$

The antenna misalignment is a state that does not vary with time, thus it remains unchanged in the time propagation step.

The error covariance matrix, $\mathbf{P}$, is also updated in discrete time according to:

$$\mathbf{P}_k^- = \mathbf{F}_{k-1} \mathbf{P}_{k-1}^+ \mathbf{F}_{k-1}^T + \mathbf{G}_{k-1} \mathbf{Q}_{\text{PSD}} \mathbf{G}_{k-1}^T \Delta t \tag{12}$$

where $\mathbf{Q}_{\text{PSD}}$ is a 6×6 diagonal matrix populated by the power spectral densities (PSDs) of the zero-mean Gaussian processes noise. Details of computing the error state matrix $\mathbf{F}$ and input mapping matrix $\mathbf{G}$, shown below, can be found in Reference 36.

$$\mathbf{F}_{k-1} = \begin{bmatrix} \mathbf{I}_{3\times3} + \frac{1}{2}\underline{\mathbf{G}}_{k-1}\Delta t^2 & \mathbf{I}_{3\times3}\Delta t & \mathbf{O}_{3\times3} \\ \underline{\mathbf{G}}_{k-1}\Delta t & \mathbf{I}_{3\times3} & \mathbf{O}_{3\times3} \\ \mathbf{O}_{3\times3} & \mathbf{O}_{3\times3} & \mathbf{I}_{3\times3} \end{bmatrix} \tag{13}$$

$$\underline{\mathbf{G}} = \left. \frac{\partial \mathbf{g}_{\mathrm{l}}}{\partial \mathbf{r}} \right|_{\mathbf{r}=\hat{\mathbf{r}}_{k-1}} \tag{14}$$

$$\mathbf{G}_{k-1} = \begin{bmatrix} -\frac{1}{2}\left(\mathbf{T}_e^b\right)^T \Delta t^2 & \mathbf{O}_{3\times3} \\ -\left(\mathbf{T}_e^b\right)^T \Delta t & \mathbf{O}_{3\times3} \\ \mathbf{O}_{3\times3} & -\mathbf{I}_{3\times3} \end{bmatrix} \tag{15}$$

B. Measurement Model

Pulsed Radars used for spacecraft navigation (e.g. the Space shuttle Ku-band radar) provide measurements of range, range rate and bearing angles to a target. We propose to extract this same information from a Synthetic Aperture Radar rather than from the returns of a tracking radar. The bearing angles to a feature on the image are determined from the SAR image itself, the range is measured directly by the radar signal processing, and in lieu of range rate we chose to

process the velocity derived from autofocus. Hence the measurement vector, $\mathbf{y}$, is given by,

$$\mathbf{y} = \begin{bmatrix} \phi_{m,1} \\ \phi_{m,2} \\ \|\mathbf{r}_{s,f}\| \\ v_{ic} \end{bmatrix} \tag{16}$$

where the individual measurement models will subsequently be explained in detail.

The two bearing measurements $\phi_{m,1}$ and $\phi_{m,2}$ cannot be extracted from a SAR image using the same algorithms employed in images generated by optical cameras since, unlike optical cameras, a SAR image is formed with radar returns at different times. The SAR image does not represent the view at one particular time through a camera with a specific field-of-view and focal length. Therefore, we do not employ a camera model to deduce bearing angles used by the navigation solution, but a different approach is developed.

The radar returns are placed at the range bin that corresponds to its distance to the satellite at the closest approach and at the azimuth line that corresponds to the zero doppler centroid.

With respect to the position of the spacecraft at one specific time, say t_m, each azimuth bin represents a displacement x_s in the azimuth direction. We define the azimuth angle as $\alpha = \arctan(x_s/z_s)$, where z_s is the slant range to the center pixel feature, see Figure 7. Notice that we are not able to extract this azimuth angle from a single return and use it as a navigation aid. Only differences in range (or phase) can be extracted from a single return, differences in azimuth are derived from the synthetic aperture.

Each range bin can also be identified by its distance y_s from the centerline of the image. We define the elevation angle as $\epsilon = \arctan(y_s/z_s)$.

Rather than bearing angles, we process tangents of angles, i.e. the measurements are:

$$\phi_{m,1} = \tan \alpha(t_m) = \frac{x_s}{z_s}, \qquad \phi_{m,2} = \tan \epsilon(t_m) = \frac{y_s}{z_s} \tag{17}$$

In summary, each pixel in the image is characterized by two coordinates that uniquely identify it. One coordinate is the time at which the azimuth angle of its returns is zero. The other is the elevation angle of the returns defined as zero at the centerline. In order to avoid explicitly calculating the elevation angles, only one pixel/feature is processed by the navigation filter: the one on the centerline. Therefore, by construction, the actual azimuth and elevation angle measurements processed by the filter are always equal to zero and they only differ by their associated time-tags.

Together with the actual measurements $\mathbf{y}$, the filter uses estimated measurements $\hat{\mathbf{y}}$ in its update step. The estimated angle measurements are not zero and require knowledge of the antenna's orientation. First, the relative vector in the

ECEF frame from the spacecraft to the center pixel feature of the SAR image is found:

$$\mathbf{r}_{s,f} = \mathbf{r}_f - \hat{\mathbf{r}}. \tag{18}$$

A graphic representation of these vectors can be seen in Figure 7. The relative position vector, $\mathbf{r}_{s,f}$, is then expressed in
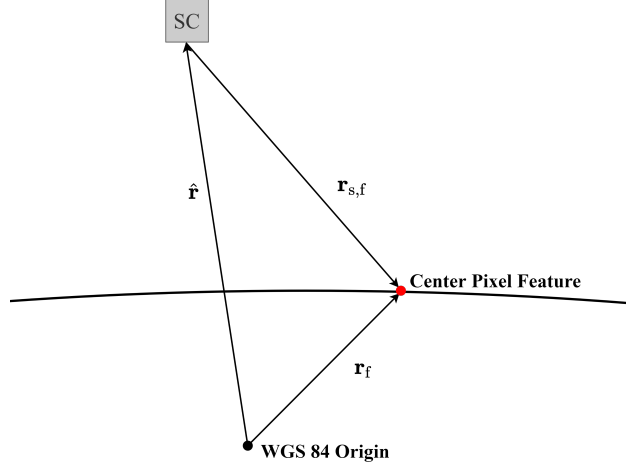

Fig. 7 Measurement vectors

the SAR antenna frame using the spacecraft attitude, estimated antenna misalignment DCM, $\hat{\mathbf{T}}_{\mu}$, and nominal DCM between spacecraft body frame and antenna frame, $\mathbf{T}_b^s$,

$$\mathbf{r}_{s,f}^s = \hat{\mathbf{T}}_{\mu} \mathbf{T}_b^s \mathbf{T}_e^b \mathbf{r}_{s,f} \tag{19}$$

where the superscript, s, on the position vector indicates that it is expressed in the antenna frame. The DCM $\mathbf{T}_b^s$ is constructed from the nominal radar look and squint angles.

The two estimated measurements can then be easily computed from $\mathbf{r}_s^s$ such that,

$$\phi_{m,1} = \frac{x_s}{z_s}, \quad \phi_{m,2} = \frac{y_s}{z_s} \tag{20}$$

where $\begin{bmatrix} x_s & y_s & z_s \end{bmatrix}^T$ are simply the components of $\mathbf{r}_{s,f}^s$. Once again, all measurements of this type are zero due to $\mathbf{r}_{s,f}^s$ only having non-zero values in the z-axis, while the predicted measurements in the filter are non-zero due to imprecise knowledge of the states.

Next, the predicted slant range to the center pixel feature is simply,

$$\text{Slant Range} \equiv \left\| \mathbf{r}_{s,f} \right\|. \tag{21}$$

The last component of the measurement vector is in-track velocity. This work focuses on near-circular orbits, with the in-track velocity of a few kilometers per second and the other two components a few meters per second. Therefore, the in-track velocity measurement is very well approximated by the velocity's magnitude. This assumption can be revisited for different types of applications. This results in the following in-track spacecraft velocity measurement model:

$$v_{ic} = \|\mathbf{v}\| . \tag{22}$$

Equations 20, 21, and 22 make up the measurement model $h(\mathbf{x})$ to be used in the measurement update of the MEKF.

C. Measurement Update

In the event that a SAR derived measurement is collected, an MEKF measurement update is performed where the first step is to calculate $\mathbf{H}_k$.

The observation model matrix, $\mathbf{H}_k$, is found by calculating the following Jacobian,

$$\mathbf{H}_k = \left. \frac{\partial h(\mathbf{x})}{\partial \mathbf{x}} \right|_{\mathbf{x}=\hat{\mathbf{x}}_k^-} . \tag{23}$$

The ratio measurement Jacobian with respect to position can be written as,

$$\frac{\partial \boldsymbol{\phi}_m}{\partial \mathbf{r}} = \frac{\partial \boldsymbol{\phi}_m}{\partial \mathbf{r}_{s,f}^s} \frac{\partial \mathbf{r}_{s,f}^s}{\partial \mathbf{r}} \tag{24}$$

where

$$\frac{\partial \boldsymbol{\phi}_m}{\partial \mathbf{r}_{s,f}^s} = \begin{bmatrix} 1/z_s & 0 & -x_s/z_s^2 \\ 0 & 1/z_s & -y_s/z_s^2 \end{bmatrix} \tag{25}$$

and

$$\frac{\partial \mathbf{r}_{s,f}^s}{\partial \mathbf{r}} = -\mathbf{T}_\mu \mathbf{T}_b^s \mathbf{T}_e^b . \tag{26}$$

The slant range measurement is only a function of vehicle position and results in the Jacobian:

$$\frac{\partial \|\mathbf{r}_{s,f}\|}{\partial \mathbf{r}} = -\frac{1}{\|\mathbf{r}_{s,f}\|} \left(\mathbf{r}_{s,f} \right)^T . \tag{27}$$

Similarly, the in-track velocity measurement is only a function of the spacecraft's velocity resulting in,

$$\frac{\partial v_{ic}}{\partial \mathbf{v}} = \frac{1}{\|\mathbf{v}\|} \left(\mathbf{v} \right)^T . \tag{28}$$

18

Finally, the Jacobian of the ratios with respect to the antenna misalignment error $\delta\boldsymbol{\mu}$ is computed from the first-order approximation of the error-attitude matrix [37],

$$\mathbf{T}\left(\delta\mathbf{q}_\mu\right) \approx \mathbf{I}_{3\times3} - [\delta\boldsymbol{\mu} \times], \tag{29}$$

yielding the Jacobian

$$\frac{\partial\boldsymbol{\phi}_m}{\partial\delta\boldsymbol{\mu}} = \frac{\partial\boldsymbol{\phi}_m}{\partial\mathbf{r}^s_{\text{s,f}}}\frac{\partial\mathbf{r}^s_{\text{s,f}}}{\partial\delta\boldsymbol{\mu}}, \tag{30}$$

where

$$\frac{\partial\mathbf{r}^s_{\text{s,f}}}{\partial\delta\boldsymbol{\mu}} = \left[\mathbf{T}_\mu\mathbf{T}^s_b\mathbf{T}^b_e\mathbf{r}_{\text{s,f}} \times\right]. \tag{31}$$

The resulting 4×9 $\mathbf{H}_k$ matrix is

$$\mathbf{H}_k = \begin{bmatrix} \frac{\partial\boldsymbol{\phi}_m}{\partial\mathbf{r}} & \mathbf{O}_{2\times3} & \frac{\partial\boldsymbol{\phi}_m}{\partial\delta\boldsymbol{\mu}} \\ \frac{\partial\|\mathbf{r}_{\text{s,f}}\|}{\partial\mathbf{r}} & \mathbf{O}_{1\times3} & \mathbf{O}_{1\times3} \\ \mathbf{O}_{1\times3} & \frac{\partial v_{ic}}{\partial\mathbf{v}} & \mathbf{O}_{1\times3} \end{bmatrix}. \tag{32}$$

Due to the measurement model employed, not all uncertainties involved are properly captured using the standard EKF implementation. Mainly, the uncertainty of the geolocation process of the SAR image is not accounted for in the measurement covariance matrix, $\mathbf{R}$, which is a diagonal matrix consisting of vector ratio, slant range, and in-track velocity errors. For example, the vector ratio and slant range measurement residuals are not simply functions of the estimated states and the direct instruments measurement noises, but have additional errors caused by the process to find the center image pixel outlined in Section IV. To account for this, a matrix, $\mathbf{B}$, is defined such that,

$$\mathbf{B}_k = \tilde{\mathbf{H}}_k\mathbf{D}\tilde{\mathbf{H}}^T_k \tag{33}$$

where $\mathbf{D}$ is the center pixel covariance matrix and $\tilde{\mathbf{H}}_k$ is the Jacobian of the measurement model with respect to the SAR image center pixel $\mathbf{r}_{\text{f}}$:

$$\tilde{\mathbf{H}}_k = \frac{\partial h(\mathbf{x})}{\partial\mathbf{r}_{\text{f}}}\bigg|_{\mathbf{x}=\hat{\mathbf{x}}^-_k} = \begin{bmatrix} -\frac{\partial\boldsymbol{\phi}_m}{\partial\mathbf{r}} \\ -\frac{\partial\|\mathbf{r}_{\text{s,f}}\|}{\partial\mathbf{r}} \\ \mathbf{O}_{1\times3} \end{bmatrix}. \tag{34}$$

Equation 33 above is very similar in structure to the $\mathbf{HPH}^T$ of the innovation covariance where $\mathbf{P}$ is transformed into the measurement space. Likewise, the uncertainty of the location of the center pixel is also transformed into the measurement space by $\tilde{\mathbf{H}}_k$, or more simply, the degree to which the uncertainty of the center pixel location impacts the

19

measurement residuals in the EKF. Additionally, in the case of this work it is assumed that the center pixel covariance matrix $\mathbf{D}$ is constant, set once and not dynamically updated. This is then included in the formulation of the innovation covariance. No feature is used more than once, this is done to avoid correlation between measurements. Unlike camera images where all the pixels are illuminated only once, SAR images are formed with many returns at different times. Using the same returns to form more the one navigation solution are purposefully avoided. Due to this, geolocation errors are seen once by the filter and can effectively be treated as white and added to the measurement noise.

The extended Kalman filter neglects higher order effects of nonlinear measurement models due to the first order Taylor approximation it utilizes. This can often cause the estimated error covariance to update too "aggressively" and become inconsistent with the true estimation error in the presence of highly accurate measurements combined with large *a priori* uncertainty [38]. Underweighting measurements is a method to account for these higher order effects by artificially increasing the measurement error to achieve consistency during filtering. Lear's method [39] accomplishes this by scaling the $\mathbf{HPH}^T$ term of the innovation covariance which accounts for the uncertainty in the states. This leads to an innovation covariance at time k of:

$$
\mathbf{S}_k = \begin{cases} (1 + \bar{\beta})\mathbf{H}_k\mathbf{P}_k^-\mathbf{H}_k^T + \mathbf{R} + \mathbf{B}_k \,, & \text{if } \sqrt{\text{tr}(\mathbf{P}_{i,k}^-)} > \gamma \\ \mathbf{H}_k\mathbf{P}_k^-\mathbf{H}_k^T + \mathbf{R} + \mathbf{B}_k \,, & \text{otherwise} \end{cases} \tag{35}
$$

where $\bar{\beta}$ and γ are tuning parameters, while $\mathbf{P}_{i,k}^-$ is a chosen partition (such as position states) of the estimation error covariance matrix. Initiating underweighting based on the partitioned covariance matrix is just one method of many. For example, one could also apply underweighting for the first n measurements after a long time span without measurement updates.

The Kalman gain is then calculated,

$$
\mathbf{K}_k = \mathbf{P}_k^-\mathbf{H}_k^T\mathbf{S}_k^{-1} \tag{36}
$$

and,

$$
\Delta\hat{\mathbf{x}}_k = \begin{bmatrix} \Delta\hat{\mathbf{r}}_k \\ \Delta\hat{\mathbf{v}}_k \\ \delta\hat{\boldsymbol{\mu}}_k \end{bmatrix} = \mathbf{K}_k\tilde{\mathbf{y}}_k \tag{37}
$$

where $\tilde{\mathbf{y}}_k$ is the pre-fit residual. Position and velocity states are updated additively:

$$
\hat{\mathbf{r}}_k^+ = \hat{\mathbf{r}}_k^- + \Delta\hat{\mathbf{r}}_k \tag{38}
$$

$$
\hat{\mathbf{v}}_k^+ = \hat{\mathbf{v}}_k^- + \Delta\hat{\mathbf{v}}_k, \tag{39}
$$

while the antenna misalignment quaternion is updated multiplicatively and re-normalized,

$$\hat{\mathbf{q}}^+_{\mu_k} = \delta\hat{\mathbf{q}}_{\mu_k} \otimes \hat{\mathbf{q}}^-_{\mu_k}, \tag{40}$$

with $\delta\hat{\mathbf{q}}_{\mu_k}$ defined as,

$$\delta\hat{\mathbf{q}}_{\mu_k} = \begin{bmatrix} \frac{\delta\hat{\mu}_k}{\|\delta\hat{\mu}_k\|} \sin\left(\frac{1}{2}\|\delta\hat{\mu}_k\|\right) \\ \cos\left(\frac{1}{2}\|\delta\hat{\mu}_k\|\right) \end{bmatrix}. \tag{41}$$

The covariance matrix is updated using the Joseph form to maintain symmetry and definiteness.

$$\mathbf{P}^+_k = (\mathbf{I}_{9\times9} - \mathbf{K}_k\mathbf{H}_k)\,\mathbf{P}^-_k\,(\mathbf{I}_{9\times9} - \mathbf{K}_k\mathbf{H}_k)^T + \mathbf{K}_k\mathbf{R}'\mathbf{K}^T_k \tag{42}$$

To account for the underweighting used above and the addition of uncertainty due to geolocation error, $\mathbf{R}'$ is defined as:

$$\mathbf{R}' = \beta\mathbf{H}_k\mathbf{P}^-_k\mathbf{H}^T_k + \mathbf{R} + \mathbf{B}_k. \tag{43}$$

VI. Numerical Simulation

The performance of the system is simulated in two ways, closed-loop and open-loop. The closed-loop simulation processes SAR data from a real spacecraft mission to generate images and derives measurements at every measurement update. The navigation solution is utilized to generate the SAR image and its associated measurements. This is in contrast to the open-loop simulation in which the SAR derived measurements are not actually generated from the methods discussed in the above section, but are simulated with errors in geolocation, in-track velocity, and range. The nominal trajectory used in the simulations and other important parameters are discussed below.

A. Closed-Loop Trajectory and SAR Data

All closed-loop Monte Carlo simulations use the same real SAR data set and hence the same nominal flight track. Namely, data from the Advanced Land Observing Satellite (ALOS) is used; a remote sensing satellite that was launched in January of 2006 by Japanese Aerospace Exploration Agency. Each Monte Carlo run disperses the initial navigation estimate as well as the slant range measurements errors. Some of the orbital parameters of ALOS can be seen in Table 2 below [40].

Table 2   ALOS orbital parameters

Orbital Parameter	Value
Altitude at equator	691.5 km
Inclination	98.16°
Eccentricity	0.00118
Period	98.5 min

A roughly 41 second trajectory from February of 2008 over the Houston area of the United States is chosen for simulation from which three images are retrieved for SAR measurement updates. What are referred here as images are technically two amplitude patches of a larger array of complex values, but for the purposes of this simulation are simply called "images".

The true trajectory of the spacecraft is known extremely well due to high-precision orbit determination performed using a duel-frequency GPS receiver together with ground control points scattered throughout the world. This results in an orbit accuracy of about 40 cm (3σ) [40]. A time history of true spacecraft attitude is generated using a multi-step approach. First, 5 pairs of position and velocity vectors are selected at equal time increments encompassing the entire trajectory. For each of these pairs, Wahba's problem is solved using singular value decomposition [41]. This method seeks to find a DCM between two coordinate systems (ECEF and body in this case) given pairs of weighted vectors. In choosing the pairs, the assumption is that the spacecraft is in an LVLH orientation and in a perfectly circular orbit. The constant spacecraft body rate is then found from the calculated attitude of the spacecraft at different times throughout the flight path and is used to create the true spacecraft attitude to be output from the simulated ADS.

Due to the fact that only one realization of real data is available for this particular orbital pass, the range measurements were corrupted with additional additive Gaussian noise in both the closed-loop simulations.

B. Open-Loop Trajectory

As discussed in the above section, only three measurement updates are included in the closed-loop trajectory. To evaluate the performance of the system for a longer trajectory (and more measurements) an open-loop simulation is conducted. Since real SAR data is not being used to generate images, synthetic measurements are derived with simulated additive zero-mean Gaussian noise.

The truth trajectory is created by using the same initial conditions as the closed-loop trajectory and propagating it forward in time under central gravity and J_2 perturbation. The spacecraft attitude is found by propagating the constant body rate previously found. This extended trajectory spans 10 minutes and the boresight ground track originates from

Houston (as in the closed-loop trajectory) ascending to northern Canada.

Simulated SAR measurements are retrieved at the same interval as the closed-loop trajectory, totaling 72 measurement updates over the 10 minute trajectory. To simulate the geolocation of the center SAR image pixel, $\mathbf{r}_f$, the (near side) intersection of a ray along the boresight of the SAR antenna and the WGS 84 ellipsoid is found at each of the measurement update times. This is done with knowledge of the true spacecraft position, attitude, and SAR pointing angles. While in the closed-loop trajectory elevation values vary, it is assumed that all feature points in the open-loop simulation are at zero elevation above the reference ellipsoid. From this, applying the proper additive Gaussian white noise yields a simulated ground center feature which can be used to calculate the two ratio measurements. Additionally, from the truth ground center feature a simulated range measurement is calculated, again with the addition of appropriate noise. Finally, instead of relying on an autofocusing algorithm for v_{ic}, the magnitude of the true velocity vector is simply calculated and noise added to simulate the measurement.

C. MEKF Parameters

During the time propagation step of the filter, only central gravity and J_2 perturbation are modeled. It is assumed that the accelerometers onboard are not sensitive enough to measure non-gravitational forces acting on the spacecraft and thus the measured body acceleration by the IMU, $\mathbf{a}_b$, is dominated by noise. Perturbing effects such as solar radiation pressure and atmospheric drag act on the spacecraft, and are accounted for in process noise added to the filter during time propagation, yielding the power spectral density matrix of,

$$\mathbf{Q}_{\text{PSD}} = \begin{bmatrix} 3.5 \times 10^{-11}\mathbf{I}_{3x3} & \mathbf{O}_{3x3} \\ \mathbf{O}_{3x3} & 3.4 \times 10^{-13}\mathbf{I}_{3x3} \end{bmatrix}$$

with process noise for the antenna misalignment states accounting for noise in the true data.

Next, the measurement covariance matrix, $\mathbf{R}$, is defined which includes the uncertainty of the two ratios, slant range, and in-track velocity measurements. It is shown below,

$$\mathbf{R} = \begin{bmatrix} \sigma^2_{\phi_{m,1}} & 0 & 0 & 0 \\ 0 & \sigma^2_{\phi_{m,2}} & 0 & 0 \\ 0 & 0 & \sigma^2_{\text{range}} & 0 \\ 0 & 0 & 0 & \sigma^2_{v_{ic}} \end{bmatrix}$$

with the respective noise standard deviations seen in Table 3.

As discussed in the measurement model section in the previous section, the two vector component ratios are always

Table 3 Measurement noise

	Value	Units
$\sigma_{\phi_{m,1}}$	0	[-]
$\sigma_{\phi_{m,2}}$	0	[-]
σ_{range}	1	m
$\sigma_{v_{ic}}$	0.54	m/s

identically zero, as the antenna boresight is aligned with the antenna frame z-axis. All the error from the zero angles measurements is due to the geolocation error and accounted for with matrices $\mathbf{D}$ and $\mathbf{B}$. For the range measurement, no data is available for the range uncertainty of the SAR instrument on ALOS, but 1 meter is chosen as this is a conservative 1σ accuracy for a radar of this type. The in-track velocity output uncertainty is obtained from experimental results of the auto-focusing algorithm outputs for a Monte Carlo simulation of the first measurement in the trajectory. It is important to note that this value is highly dependent on the step size used for focusing, with small steps yielding more accurate in-track velocity measurements. For the closed-loop simulation this step size is fixed at 1 m/s.

Similarly to the uncertainty of the in-track velocity measurement, the center pixel covariance matrix, $\mathbf{D}$, introduced in Equation 33 is found using Monte Carlo simulations of the first measurement with ECEF uncertainty ranging from 2 to 8 meters 1σ. This covariance matrix accounts the uncertainty due to the geolocation process and is used to generate zero mean additive Gaussian noise to simulate geolocation error in the open-loop simulation. In reality, it is likely that this geolocation error is position dependent in regards to the amount of error in each direction due to the view of the ECEF coordinate system changing from the perspective of the SAR antenna. For the purposes of this paper, it is assumed that this geolocation covariance matrix is constant.

Underweighting is only utilized in test case 1, as it is found to be necessary in that scenario only. A description of the two test cases is discussed in a later section. In test case 1, underweighting of measurements is applied based on the measurement index and not the filter's predicted uncertainty. The first 10 measurements are chosen to have underweighting applied as this is when filter inconsistency is most likely to occur due to the reception of low uncertainty measurements after a period lacking any measurements. Since the closed-loop simulation only has three measurement updates, each of them has underweighting applied for test case 1. The underweighting parameter, $\bar{\beta}$, is chosen to be 0.2, the same value used for the Space Shuttle [39]. In the open-loop simulation the propagation phase of the filter runs at 100Hz, while in the closed loop simulation it occurs at a rate of approximately 2200 Hz. While propagation at such high rate is un-necessary and an onboard implementation will use the same algorithms at a much lower frequency, this value was chosen as it matches the available trajectory orbit data. Both the closed and open-loop simulations have measurement updates occurring every 8.2 seconds or 0.12 Hz.

VII. Test Cases

Two test cases are simulated which only differ in the uncertainty of the initial state estimates, while keeping all other parameters discussed in the previous sections identical. Specifically, both cases begin with the same initial uncertainty for the position and velocity states, but a different uncertainty for the initial antenna misalignment. The chosen misalignment of 0.1 deg is a commonly used value, see for example the antenna misalignment in [42]. The more accurate value of 0.01 degrees was chosen as an example of what could happen if the two sensors are mounted on a common navigation base with accurate pre-flight alignment.

A table of the initial estimation errors of the two test cases is seen below. This uncertainty is applied to all components of the respective states. It is therefore important to notice that the velocity error is applied in all directions, not the in-track direction only, the results show that a focused image is still obtained for this level of navigation velocity uncertainty.

Table 4   Initial estimation error

State	TC-1 Initial Uncertainty $[1\sigma]$	TC-2 Initial Uncertainty $[1\sigma]$	Units
r	1000	1000	m
v	10	10	m/s
μ	0.1	0.01	deg

A. Monte Carlo Results

Two sets of plots are shown for the test case 1 scenario, where sample statistic results are constructed from 100 Monte Carlo runs. Figures 8a - 8c show results of the closed-loop simulation for three measurement updates where the error of each run is shown as a gray line with the dashed black line representing the sample mean of the estimation error. This mean error is nearly zero throughout the trajectory meaning the filter produces unbiased estimates. The filter predicted estimation error covariance (3σ) is plotted with the sample error covariance (3σ) in red and green respectively. The sample covariance shows the true error characteristics, which the filter attempts to estimate. When these two covariances match closely, the filter is said to be consistent and this can be seen in the figures as well. Although not explicitly shown, there is very good agreement between the closed-loop and open-loop simulation results for the measurements that are common to both. Once again, Figures 8a - 8c are obtained extracting measurements from SAR images created with real data and the estimated navigation values.

Figures 9a - 9c show the same information as Figures 8a - 8c except now the open-loop trajectory is shown for the full 10 minute time span. The sample and predicted covariances generally have good agreement. At the end of the trajectory the uncertainty (1σ) for the ECEF position ranges from roughly 20 meters in the x-axis to 740 meters in the y-axis, a 98% and 26% decrease respectively.

The same sets of figures are presented for test case 2 as for test case 1. In Figures 10a - 10c the closed-loop simulation results show unbiased estimation along with acceptable filter consistency. Additionally, while again not shown, there is good agreement between the open-loop and closed-loop simulation as the sample uncertainties of the first three measurements match closely. Finally, Figures 11a - 11c show unbiased estimation and good consistency throughout the 10 minute open-loop trajectory. The ECEF positional uncertainty (1σ) at the end of the trajectory ranges from 12 meters in the x-axis to 138 meters in the y-axis, a 98.8% and 86.2% decrease respectively. As expected, for both test cases, antenna misalignment uncertainty around the antenna z-axis (boresight) does not decrease due to the lack of observability of this component because of measurement types employed. The largest difference between the two test cases that can be seen is that when the initial antenna misalignment uncertainty is low (as in test case 2) the position and velocity state errors decrease rapidly to their steady state values, while antenna misalignment uncertainty only decreases slightly during this 10 minute section of the orbit.
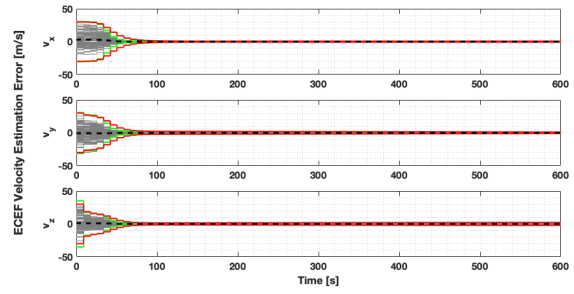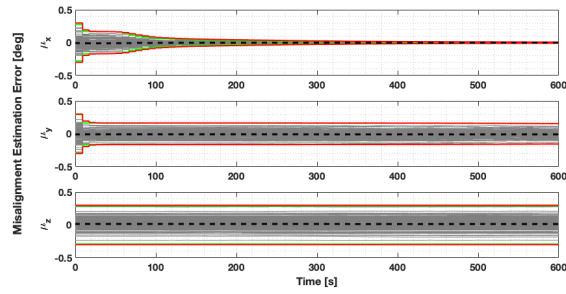

(a) Position estimation

(b) Velocity estimation

(c) Antenna misalignment estimation
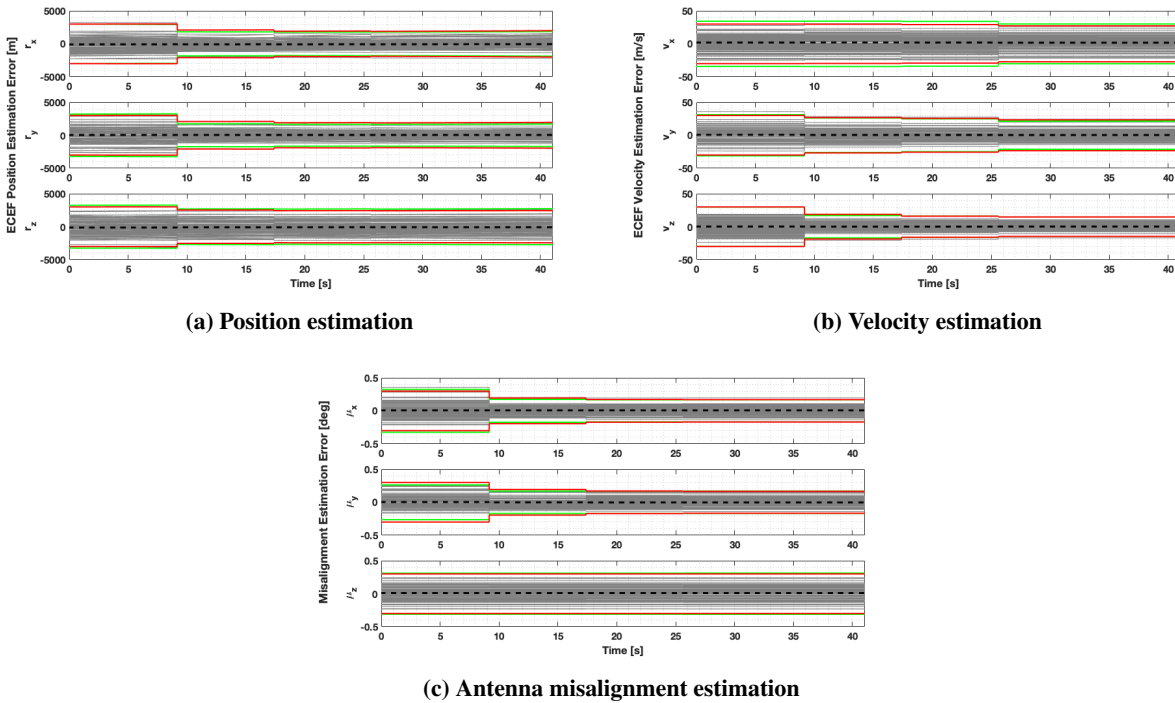
Fig. 8   Monte Carlo results of closed-loop estimation error (TC-1)
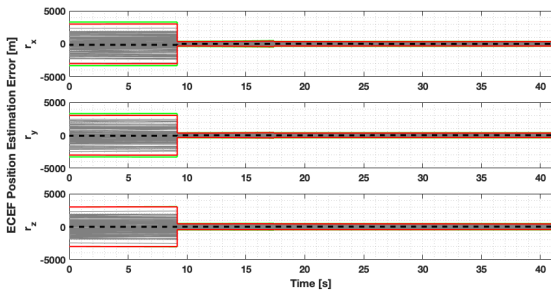
26
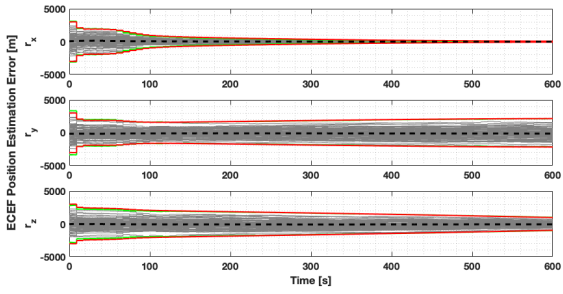
(a) Position estimation

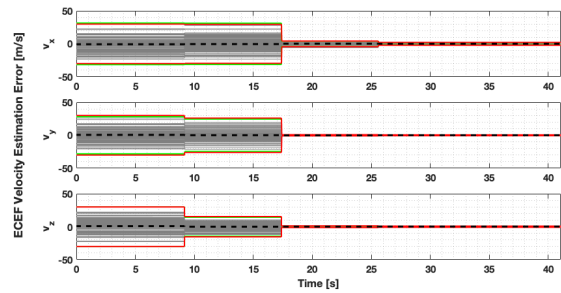(b) Velocity estimation

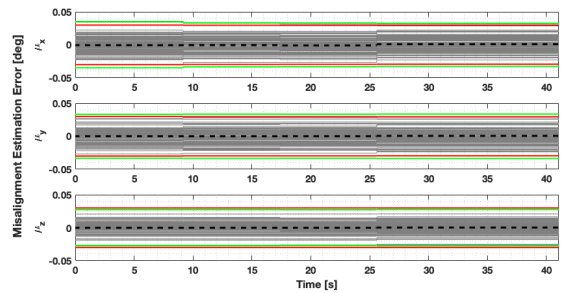(c) Antenna misalignment estimation

Fig. 9   Monte Carlo results of open-loop estimation error (TC-1)

(a) Position estimation

(b) Velocity estimation

(c) Antenna misalignment estimation

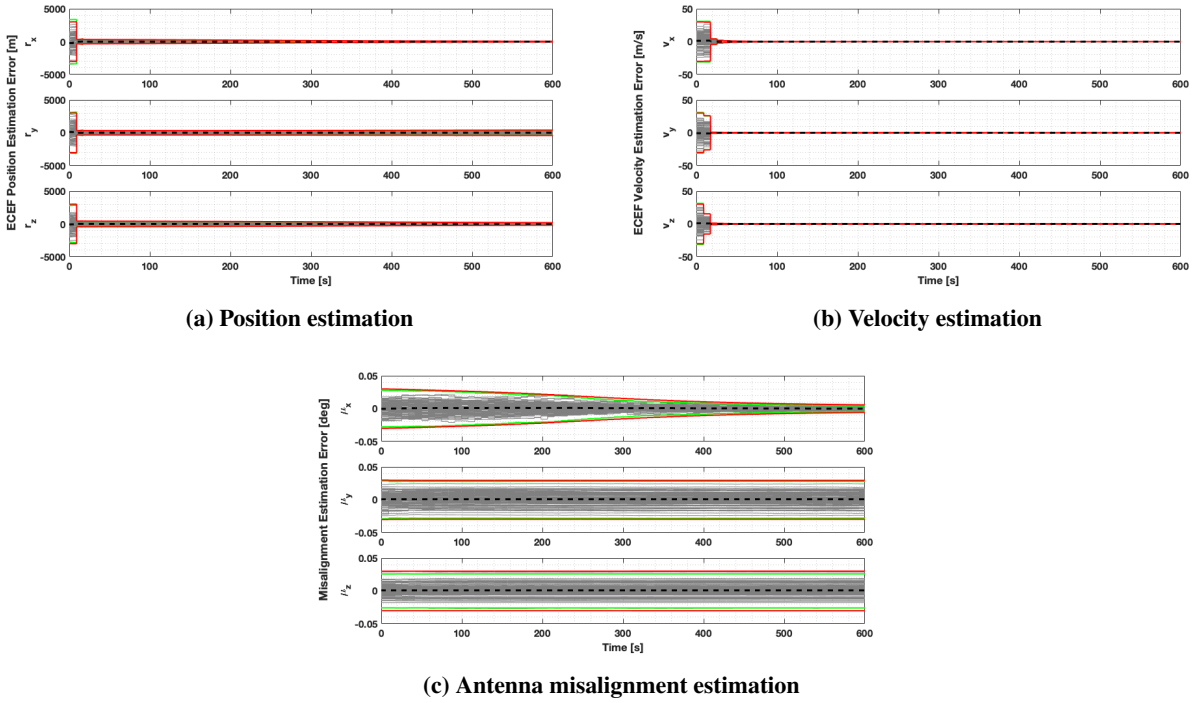**Fig. 10   Monte Carlo results of closed-loop estimation error (TC-2)**

(a) Position estimation

(b) Velocity estimation

(c) Antenna misalignment estimation

Fig. 11   Monte Carlo results of open-loop estimation error (TC-2)

VIII. Conclusion

A prototype SAR based terrain relative navigation system has been proposed and developed. A key component of this work is the fact that this is a closed-loop navigation architecture where the SAR measurements and navigation filter are reliant on one another. Through Monte Carlo analysis of the MEKF performance for two test cases, it was shown that the filter bounds and often significantly reduces state errors throughout the trajectory. In the comparison of the two test cases, it is clear that a smaller initial antenna misalignment error has a significant contribution to the rate that the other two states' uncertainty decreases, which is an expected result due to the direct downstream coupling of antenna misalignment with position and velocity EKF measurement updates.

Acknowledgment

References

[1] Golden, J. P., "Terrain contour matching (TERCOM): A cruise missile guidance aid," <u>Image processing for missile guidance,</u> Vol. 238, International Society for Optics and Photonics, 1980, pp. 10–18. https://doi.org/10.1117/12.959127.

[2] McGee, T. G., Rosendall, P. E., Hill, A., Shyong, W. J., Criss, T. B., Reed, C., Chavers, G., Hannan, M., Epp, C., and Nishant, M., "APLNav: Development status of an onboard passive optical terrain relative navigation system," <u>AIAA Guidance, Navigation, and Control Conference,</u> 2015, p. 0853. https://doi.org/10.2514/6.2015-0853.

[3] Rutishauser, D., Epp, C., and Robertson, E., "Free-flight terrestrial rocket lander demonstration for NASA's Autonomous Landing and Hazard Avoidance Technology ALHAT system," <u>AIAA SPACE 2012 Conference & Exposition,</u> 2012, p. 5239. https://doi.org/10.2514/6.2012-5239.

[4] Mastrodemos, N., Rush, B., Vaughan, D., and Owen, B., "Optical navigation for Dawn at Vesta," <u>21st AAS/AIAA Space Flight Mechanics Meeting,</u> 2011. AAS 11-222.

[5] Johnson, A. E., and Montgomery, J. F., "Overview of terrain relative navigation approaches for precise lunar landing," <u>2008 IEEE Aerospace Conference,</u> IEEE, 2008, pp. 1–10. https://doi.org/10.1109/AERO.2008.4526302.

[6] Amzajerdian, F., Roback, V. E., Bulyshev, A. E., Brewster, P. F., Carrion, W. A., Pierrottet, D. F., Hines, G. D., Petway, L. B., Barnes, B. W., and Noe, A. M., "Imaging flash LIDAR for safe landing on solar system bodies and spacecraft rendezvous and docking," <u>Laser Radar Technology and Applications XX; and Atmospheric Propagation XII,</u> Vol. 9465, International Society for Optics and Photonics, 2015, p. 946502. https://doi.org/10.1117/12.2178410.

[7] Roy, D. P., Wulder, M. A., Loveland, T. R., Woodcock, C. E., Allen, R. G., Anderson, M. C., Helder, D., Irons, J. R., Johnson, D. M., Kennedy, R., et al., "Landsat-8: Science and product vision for terrestrial global change research," <u>Remote sensing of Environment,</u> Vol. 145, 2014, pp. 154–172. https://doi.org/10.1016/j.rse.2014.02.001.

[8] Born, G., Dunne, J., and Lame, D., "Seasat mission overview," <u>Science,</u> Vol. 204, No. 4400, 1979, pp. 1405–1406. https://doi.org/10.1126/science.204.4400.1405.

[9] Werner, M., "Shuttle radar topography mission (SRTM) mission overview," <u>Frequenz,</u> Vol. 55, No. 3-4, 2001, pp. 75–79. https://doi.org/10.1515/freq.2001.55.3-4.75.

[10] Geudtner, D., Torres, R., Snoeij, P., Davidson, M., and Rommen, B., "Sentinel-1 system capabilities and applications," <u>2014 IEEE Geoscience and Remote Sensing Symposium,</u> IEEE, 2014, pp. 1457–1460. https://doi.org/10.1109/igarss.2014.6946711.

[11] Bevington, J. E., and Marttila, C. A., "Precision aided inertial navigation using SAR and digital map data," <u>IEEE Symposium on Position Location and Navigation. A Decade of Excellence in the Navigation Sciences,</u> IEEE, 1990, pp. 490–496. https://doi.org/10.1109/PLANS.1990.66219.

[12] Paschall, R. N., and Layne, J., "Design and analysis of an integrated targeting system," <u>Proceedings of National Aerospace and Electronics Conference (NAECON'94),</u> IEEE, 1994, pp. 937–944. https://doi.org/10.1109/NAECON.1994.332939.

[13] Doerry, A. W., "Estimating IMU heading error from SAR images." Tech. rep., Sandia National Laboratories, 2009. https://doi.org/10.2172/952099.

[14] Doerry, A. W., Horndt, V., Bickel, D. L., and Naething, R. M., "Estimating Radar Velocity using Direction of Arrival Measurements," Tech. rep., Sandia National Laboratories, 2014. https://doi.org/10.2172/1323271.

[15] Nitti, D. O., Bovenga, F., Chiaradia, M. T., Greco, M., and Pinelli, G., "Feasibility of using synthetic aperture radar to aid UAV navigation," Sensors, Vol. 15, No. 8, 2015, pp. 18334–18359. https://doi.org/10.3390/s150818334.

[16] Kim, Y., Park, J., and Bang, H., "Terrain-referenced navigation using an interferometric radar altimeter," NAVIGATION, Journal of the Institute of Navigation, Vol. 65, No. 2, 2018, pp. 157–167. https://doi.org/10.1002/navi.233.

[17] Christensen, R. S., Gunther, J., and Long, D., "Toward GPS-denied Navigation Utilizing Back Projection-based Synthetic Aperture Radar Imagery," ION 2019 Pacific PNT Meeting, Honolulu, Hawaii, 2019, pp. 108–119. https://doi.org/10.33012/2019.16797.

[18] Lindstrom, C., Christensen, R., and Gunther, J., "An investigation of GPS-denied navigation using airborne radar telemetry," 2020 IEEE/ION Position, Location and Navigation Symposium (PLANS), 2020, pp. 168–176. https://doi.org/10.1109/plans46316.2020.9110233.

[19] Grewal, M., and Andrews, A., "How good is your gyro [ask the experts]," IEEE Control Systems Magazine, Vol. 30, No. 1, 2010, pp. 12–86. https://doi.org/10.1109/mcs.2009.935122.

[20] White, T., Wheeler, J., Lindstrom, C., Christensen, R., and Moon, K. R., "GPS-Denied Navigation Using SAR Images and Neural Networks," arXiv preprint arXiv:2010.12108, 2020. https://doi.org/10.1109/icassp39728.2021.9414421.

[21] Moreira, A., Prats-Iraola, P., Younis, M., Krieger, G., Hajnsek, I., and Papathanassiou, K. P., "A tutorial on synthetic aperture radar," IEEE Geoscience and remote sensing magazine, Vol. 1, No. 1, 2013, pp. 6–43. https://doi.org/10.1109/MGRS.2013.2248301.

[22] Cumming, I. G., and Wong, F. H., Digital processing of synthetic aperture radar data: algorithms and implementation, Artech House Norwood, MA, 2005.

[23] JAXA/METI, "ALOS PALSAR L1.0," , 2008. Accessed through ASF DAAC 04 April 2020.

[24] Groen, F. C., Young, I. T., and Ligthart, G., "A comparison of different focus functions for use in autofocus algorithms," Cytometry: The Journal of the International Society for Analytical Cytology, Vol. 6, No. 2, 1985, pp. 81–91. https://doi.org/10.1002/cyto.990060202.

[25] MATLAB, Computer Vision Toolbox, The MathWorks, Inc., Natick, Massachusetts, United States, 2020. URL https://www.mathworks.com/products/computer-vision.html.

[26] Bay, H., Tuytelaars, T., and Van Gool, L., "Surf: Speeded up robust features," European conference on computer vision, Springer, 2006, pp. 404–417. https://doi.org/10.1007/11744023_32.

[27] Torr, P. H., and Zisserman, A., "MLESAC: A new robust estimator with application to estimating image geometry," Computer vision and image understanding, Vol. 78, No. 1, 2000, pp. 138–156. https://doi.org/10.1006/cviu.1999.0832.

[28] Durgam, U. K., Paul, S., and Pati, U. C., "SURF based matching for SAR image registration," 2016 IEEE Students' Conference on Electrical, Electronics and Computer Science (SCEECS), IEEE, 2016, pp. 1–5. https://doi.org/10.1109/sceecs.2016.7509292.

[29] Liu, R., and Wang, Y., "SAR image matching based on speeded up robust feature," 2009 WRI Global Congress on Intelligent Systems, Vol. 4, IEEE, 2009, pp. 518–522. https://doi.org/10.1109/gcis.2009.297.

[30] Suri, S., Schwind, P., Uhl, J., and Reinartz, P., "Modifications in the SIFT operator for effective SAR image matching," International Journal of Image and Data Fusion, Vol. 1, No. 3, 2010, pp. 243–256. https://doi.org/10.1080/19479832.2010.495322.

[31] Strozzi, T., Luckman, A., Murray, T., Wegmuller, U., and Werner, C. L., "Glacier motion estimation using SAR offset-tracking procedures," IEEE Transactions on Geoscience and Remote Sensing, Vol. 40, No. 11, 2002, pp. 2384–2391. https://doi.org/10.1109/tgrs.2002.805079.

[32] Shuster, M. D., "Survey of attitude representations," Journal of the Astronautical Sciences, Vol. 41, 1993, pp. 439–517.

[33] Zanetti, R., "Rotations, Transformations, Left Quaternions, Right Quaternions?" The Journal of the Astronautical Sciences, Vol. 66, No. 3, 2019, pp. 361–381. https://doi.org/10.1007/s40295-018-00151-2.

[34] Markley, F. L., "Attitude estimation or quaternion estimation?" Journal of the Astronautical Sciences, Vol. 52, No. 1-2, 2004, pp. 221–238. https://doi.org/10.1007/BF03546430.

[35] Titterton, D., Weston, J. L., and Weston, J., Strapdown inertial navigation technology, Vol. 17, IET, 2004. https://doi.org/10.1049/PBRA017E.

[36] Zanetti, R., "Advanced navigation algorithms for precision landing," Ph.D. thesis, The University of Texas at Austin, 2007.

[37] Crassidis, J. L., and Junkins, J. L., Optimal estimation of dynamic systems, CRC press, 2011. https://doi.org/10.1201/9780203509128.

[38] Carpenter, J. R., and D'Souza, C. N., "Navigation filter best practices," Tech. rep., NASA Langley Research Center, 2018.

[39] Lear, W. M., "Multi-phase navigation program for the Space Shuttle Orbiter," JSC Internal Note No. 73-FM-132, 1973.

[40] Shimada, M., Tadono, T., and Rosenqvist, A., "Advanced Land Observing Satellite (ALOS) and monitoring global environmental change," Proceedings of the IEEE, Vol. 98, No. 5, 2009, pp. 780–799. https://doi.org/10.1109/jproc.2009.2033724.

[41] Markley, F. L., "Attitude determination using vector observations and the singular value decomposition," Journal of the Astronautical Sciences, Vol. 36, No. 3, 1988, pp. 245–258.

[42] Tom G. Farr et al, "The Shuttle Radar Topography Mission," Reviews of Geophysics, Vol. 45, No. 2, 2007. https://doi.org/10.1029/2005RG000183.